COEXISTENCE OF SOLID AND SUPERCOOLED LIQUID. THERMODYNAMIC EQUILIBRIUM AND DYNAMICS

A Thesis

Presented to the Faculty of the Graduate School

of Cornell University

in Partial Fulfillment of the Requirements for the Degree of

Master of Science

by

Antoine Marc Jean Robin

August 2018

ABSTRACT

We study the thermodynamic equilibrium between supercooled liquid and solid using a homemade MEMS device called microtensiometer to directly measure the pressure and temperature of a macroscopic volume of supercooled liquid in equilibrium with solid. Our measurements on water are consistent with the generalized Clapeyron equation, which predict the relation between the pressure of the liquid, the pressure of the solid and the temperature at equilibrium. We also report and discuss remarkable behaviors in the kinetics of equilibration. We found that the equilibration time to reach chemical equilibrium can vary by several orders of magnitude. To better understand this observation, we do a more careful study of the dynamics of transport of supercooled water into ice using a custom-made microfluidic platform. Our results indicate that the dynamics is slower than the prediction of the generalized Clapeyron equation, assuming that the ice remains at atmospheric pressure. We speculate that the transport impacts the pressure in the ice and leads to an effectively lower driving force.

BIOGRAPHICAL SKETCH

Antoine obtained his bachelor degree in physics at École Normale Supérieure de Cachan (France) in 2014. He then obtained the Agrégation de physique chimie (French master degree in teaching of physics and chemistry) in 2016. Antoine began his PhD in 2016 at Cornell University under the supervision of Drs. Abraham Duncan Stroock (Chemical Engineering, Ithaca), Fernando Escobedo (Chemical Engineering, Ithaca) and Robert Thorne (Physics, Ithaca).

To Dianea Alice Kohl, for her love.

ACKNOWLEDGEMENTS

I would first like to thank my advisor Dr. Abraham Stroock for his inspiring mentorship and constant support. I would also like to thank my committee members, Dr. Robert Thorne and Fernando Escobedo for their discussions and guidance. I am grateful to Al Kovaleski and Jason Londo for their collaboration on a project to study supercooling in grapevine buds.

I am also grateful to my research colleagues. Piyush Jain for his friendship and unconditional support in difficult moments, Olivier Vincent for our trips to nature and scientific discussions, Pierre Lidon for our discussions, Michael Santiago for the three weeks we happily spent in the cleanroom. I also thank Siyu Zhu, Hanwen Lu and Winston Black for their daily benevolence and invaluable help.

CONTENTS

Biographical Sketch . . . iii
Dedication . . . iv
Acknowledgements . . . v
Contents . . . vi
List of Figures . . . viii

1 Introduction **1**

2 Background **2**
2.1 Supercooled liquids . . . 2
2.2 Freezing point depression in confinement . . . 3
2.2.1 Freezing temperature and Gibbs-Thomson equation . . . 3
2.2.2 Pressure in the liquid . . . 6
2.2.3 Ice meniscus . . . 7

3 Contexts **9**
3.1 Soils and frost heave . . . 9
3.2 Cold hardiness in plants . . . 10
3.2.1 Freeze tolerance . . . 11
3.2.2 Freeze avoidance . . . 12
3.3 Porous solids . . . 13

4 Study on water **16**
4.1 Theory . . . 16
4.2 Materials and Methods . . . 19
4.2.1 Description and working principle of microtensiometer . . . 19
4.2.2 Fabrication, calibration and packaging . . . 21
4.2.3 Experiment . . . 24
4.3 Results and discussion . . . 25
4.3.1 Thermodynamic equilibrium . . . 25
4.3.2 Kinetics . . . 27
4.3.3 Failure of the microtensiometer . . . 29

5 Study on Acetic Acid **31**

6 Transport of supercooled liquid into the frozen phase **33**
6.1 Materials and Methods . . . 33
6.2 Results and discussion . . . 34

7 Future work **36**
7.1 Study of cryogenic swelling . . . 36
7.2 Study on doubly metastable liquid . . . 37

8 Conclusion **38**

Bibliography **39**

LIST OF FIGURES

2.1 Phase diagram of water 2
2.2 Freezing point depression in confinement 3
2.3 Freezing point depression of water 4

3.1 Basic mechanism of frost heave 9
3.2 Supercooling in xylem of shagbark hickory tree 11
3.3 Crysuction and cryogenic swelling 13
3.4 Deformation of a water saturated porous media in equilibrium with bulk ice 14

4.1 Theoretical pressure in supercooled water in equilibrium with ice . 16
4.2 Extended phase diagram of water 17
4.3 Description and working principle of microtensiometer 20
4.4 Packaging of a sensor 22
4.5 Pressure calibration 23
4.6 Temperature calibration 24
4.7 Experimental setup 25
4.8 Pressure in the liquid Versus Temperature at equilibrium 26
4.9 Pressure transient 27
4.10 Failure of the microtensiometer 30

5.1 Experiment with acetic acid 31

6.1 Study of the cryosuction dynamics 33
6.2 Cryosuction dynamics 34

7.1 Study of cryogenic swelling with a microtensiometer 36

CHAPTER 1

INTRODUCTION

Coexistence of solid and supercooled liquid (i.e. liquid colder than bulk freezing temperature) has important consequences in a variety of contexts. Liquid saturated concrete swells and cracks at subfreezing temperature, causing severe damage to roads and buildings. In soils, warm water from the ground water migrates towards frozen region, causing an upwards displacement of the soil that disrupts infrastructures. Also, plants that live in cold regions are able to survive winter thanks to extracellular ice, which is used to pull liquid out of living cells to preserve them from freezing. It is a well-known fact that confined liquids freeze at lower temperature than the bulk and the depression of the freezing point has been extensively characterized. However, little attention has been devoted to the liquid phase when it coexists with the solid. Better understanding of solid/supercooled liquid equilibrium is crucial to improve protection of infrastructures and crops against frost damage. In this thesis, we help filling this gap in the literature by providing direct measurements of the pressure of a macroscopic volume of liquid in equilibrium with the solid phase at different degrees of supercooling. We show that as the temperature drops and the liquid gets more supercooled, its pressure decreases and becomes negative. We also provide comprehensive theoretical calculations of the state of the liquid, which very well reproduces the experimental data. The experiments were done using a homemade MEMS device called a microtensiometer, in which a macroscopic volume of liquid can equilibrate with the solid phase through a nano-porous membrane.

CHAPTER 2

BACKGROUND

2.1 Supercooled liquids

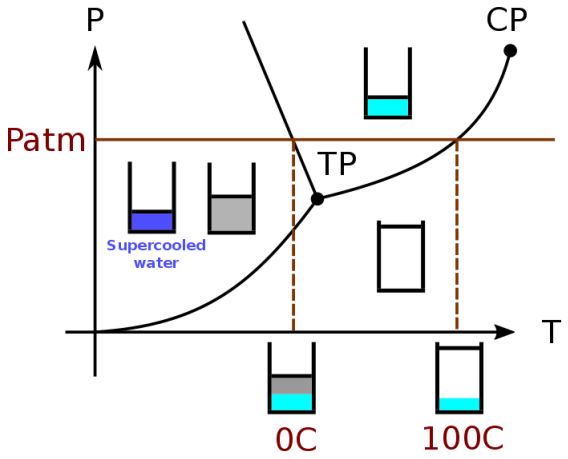

Figure 2.1: Phase diagram of water. Water at a pressure of 1 bar is supercooled when its temperature is lower than the corresponding freezing temperature: 0 °C.

A volume of liquid at pressure P_l is supercooled when its temperature is such that $T_l \leq T_0(P_l)$, where T_0 is the temperature of coexistence of liquid and solid. For example, water at 1 bar is supercooled when its temperature is less than 0 °C (see Figure 2.1). Supercooling is a metastable state, any small perturbation will trigger freezing. In practice, moderate supercooling can be easily achieved if the container has smooth, clean walls and care is taken not to mechanically disturb the liquid. Physically, supercooling exists because the nucleation of the ice phase requires to overcome an energy barrier. This energy barrier decreases with increasing supercooling. At the temperature of nucleation, the barrier can be overcome and the water freezes spontaneously. The energy barrier depends on the freezing process. The highest energy barrier corresponds to homogeneous nucleation where the ice nucleates in the bulk liquid. For water, the temperature of homogeneous

nucleation is $-38\,°C$. This energy barrier can be significantly decreased if the solid nucleates on a hydrophobic surface (heterogeneous nucleation). In practise, it is difficult to supercool water to the temperature of homogeneous nucleation.

2.2 Freezing point depression in confinement

2.2.1 Freezing temperature and Gibbs-Thomson equation

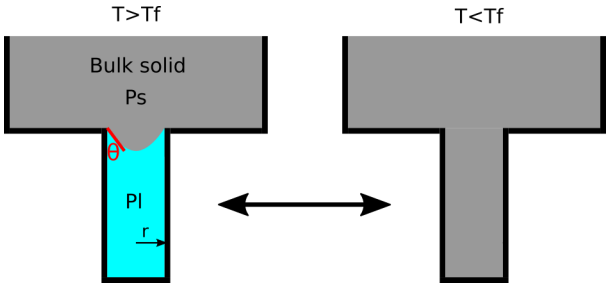

Figure 2.2: Freezing point depression in confinement. The liquid is confined in a cylindrical pore of radius r and the pore mouth is covered with macroscopic ice at pressure P_s. The freezing transition occurs at temperature T_f which is lower than the bulk equilibrium temperature. $T_f \leq T_0(P_s)$. When the temperature is above Tf, the interface between the liquid and the solid forms a meniscus. θ is the angle between the wall the interface.

In confined media, the freezing point is depressed relative to the bulk when the liquid wets the wall [2]. More precisely, liquid confined in a narrow pore open to macroscopic solid will freeze at lower temperature than the bulk (see Figure 2.2). This can be explained by a simple thermodynamic argument. The freezing point depression comes from the non-negligible contribution of the interfacial energies to the Gibbs Free Energy relative to the volumetric term, which modifies the equilibrium. This phenomenon is typical in porous media. For example, freezing point depression is similar to capillary evaporation, where liquid confined in a pore open to vapor evaporates at a lower vapor pressure than the bulk saturation

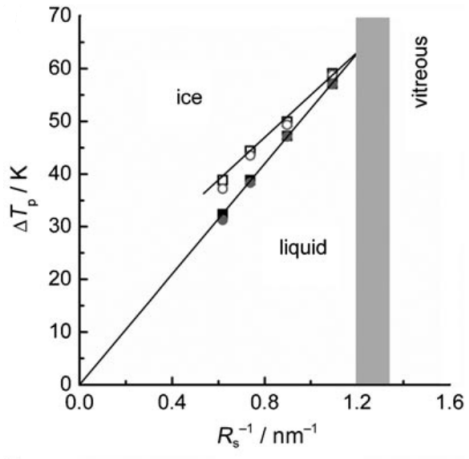

Figure 2.3: Freezing point depression of water (reproduced from [1]). Freezing point depression (open symbols) and melting point depression (full symbols) of water in cylindrical silica nano-pores measured by DSC. Rs is an effective radius equal to $Rs = R - t$ where R is the radius of the pore and t is interpreted as the thickness of a non-freezing layer. This non-freezing layer is typically two monolayers of water molecules thick. With this correction, the data is in very good agreement with the Gibbs-Thomson equation.

pressure.

The freezing temperature T_f can be found by comparing the Gibbs free energies of the frozen and unfrozen states (which would be respectively the right and left drawings in Figure 2.2).

$$\Delta G = \Sigma(\gamma_{SW} - \gamma_{LW}) + \Delta G_s + \Delta G_l \tag{2.1}$$

$$\Delta G = \Sigma(\gamma_{SW} - \gamma_{LW}) + n(\mu_s - \mu_l) \tag{2.2}$$

When ΔG changes sign, the solid becomes the favored phase in the pore. Therefore, T_f is such that $\Delta G = 0$

$$\mu_s - \mu_l = \frac{\Sigma}{n}(\gamma_{SW} - \gamma_{LW}) \tag{2.3}$$

$$\mu_s - \mu_l = \frac{\Sigma}{V} v_l(\gamma_{SW} - \gamma_{LW}) \tag{2.4}$$

Where Σ is the inner surface of the pore, γ_{SW} is the interfacial energy of the solid and the wall, γ_{LW} is the interfacial energy of the liquid and the wall, n is the number of moles of liquid, V is the volume of the pore, v_l is the molar volume of liquid.

The bulk equilibrium corresponds to $\Delta\mu = 0$. We can see how the confinement shifts the bulk equilibrium. Indeed, the shift will be more dramatic the greater the surface to volume ratio. Also, it makes sense that the shift is proportional to the differences in interaction between the phases and the wall. Physically, one phase has to interact more favorably with the wall than the other to influence the equilibrium. Eq. (2.4) is the exact expression of the Gibbs-Thomson equation. Approximations can be made to extract an explicit expression of T_f.

$$\mu_s - \mu_l \approx (s_l - s_s)(T_f - T_0) \tag{2.5}$$

$$\mu_s - \mu_l \approx -\frac{l_f}{T_0}(T_0 - T_f) \tag{2.6}$$

$$T_f - T_0 = \frac{\Sigma}{V}\frac{T_0 v_l(\gamma_{SW} - \gamma_{LW})}{l_f} \tag{2.7}$$

Where l_f is the molar enthalpy of fusion. For a cylindrical pore, the freezing point depression is equal to:

$$T_f - T_0 = \frac{2}{r}\frac{T_0 v_l(\gamma_{SW} - \gamma_{LW})}{l_f} \tag{2.8}$$

Equation (2.8) is known as the Gibbs-Thomson equation [2]. It predicts that the freezing point depression is inversely proportional to the radius of the pore. The freezing of confined water has been measured in pores of well defined geometry by Findegg et al [1]. As shown in Figure 2.3, their data agree quantitatively with the Gibbs-Thomson equation. Their experiment also suggests the existence of a non-freezable layer of liquid adjacent to the pore wall. A lot of research has been done on this so-called premelted layer which reveals that solids have a liquid-like surface film at temperature below the bulk melting temperature [3]. The thickness of the film increases as temperature approaches the bulk metling point. The premelted layer is thought to play an important role in numerous phenomena such as ice friction, frost heave, glaciers, thunderstorms, destruction of ozone.

2.2.2 Pressure in the liquid

For $T > Tf$, the liquid does not freeze even though the mouth of the pore is covered with macroscopic ice. So far, we have characterized the freezing temperature Tf but we can ask what is the pressure of the liquid confined in the pore? Not a lot of research has been done to measure the pressure of the confined liquid and there is a gap in the literature. So far, the most thorough study has been done by Erko and al. (Figure 3.4) who measured the stress exerted by confined water on the porous matrix [4].

It is important to recognize that the two phases can exchange matter and should be in chemical equilibrium. Thermodynamics requires identity of the chemical

potentials. It is obvious that the liquid cannot be at the same pressure as the solid because this is can only happen at $T = T_0$. We have

$$\mu_s(P_s, T) = \mu_l(P_l, T) \tag{2.9}$$

Equilibrium is characterized by three parameters, only two of which are independent. Implicitly, equation (2.9) yields a relation $P_l = P_l(P_s, T)$. Qualitatively, because $T < T_0$, $\mu_l(P_s, T) \geq \mu_s(P_s, T)$, so we have $\mu_l(P_s, T) \geq \mu_l(P_l, T)$. Because the chemical potential increases with pressure, we must have $P_l < P_s$. Therefore, we expect that the liquid decreases its pressure to sustain equilibrium. The same happens for a liquid confined in a pore open to vapor.

Equation (2.9) should not be confused with the Clapyeron equation, which characterizes equilibrium between two bulk phases which are at the same pressure: $\mu_s(P, T) = \mu_l(P, T)$. The Clapeyron equation allows to compute the binodals lines $P(T)$ of the phase diagram. To avoid confusion, (2.9) is usually referred to as the generalized Clapeyron equation.

2.2.3 Ice meniscus

The discontinuity of pressure at the interface between the two phases must be mechanically sustained. Evidence of a curved ice meniscus can be found in the literature [5]. It has been speculated the [6] that curvature the follows Laplace law.

$$P_s - P_l = \frac{2\gamma_{SL}\cos\theta}{r} \tag{2.10}$$

Where γ_{SL} is the solid/liquid surface tension and θ is the angle of the solid/liquid interface with the pore wall. A drawing of the interface is presented in Figure 2.2.

CHAPTER 3

CONTEXTS

When a system containing solid and supercooled liquid is initially not in equilibrium, transfer of matter occurs to homogenize the chemical potential. The transfer of matter modifies the pressure of the different phases, until either one of them disappear, or the difference of their chemical potential is cancelled. The nature of the system gives rise to variety of phenomena.

3.1 Soils and frost heave

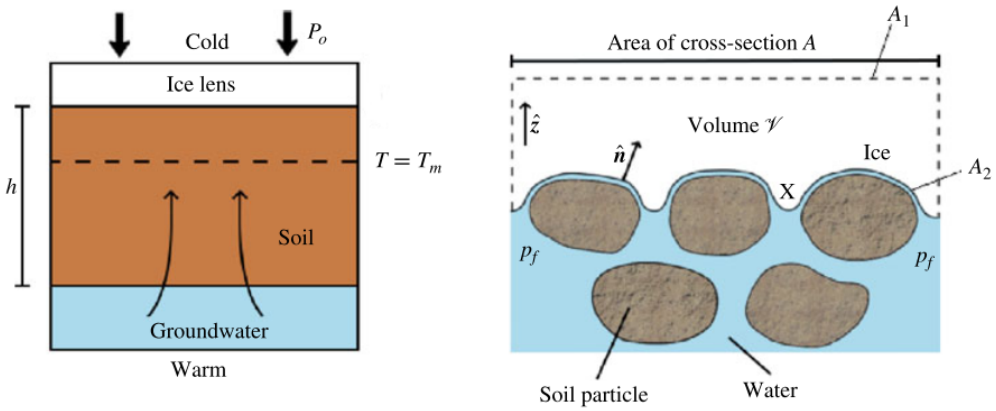

Figure 3.1: Basic mechanism of frost heave. (Reproduced from [7]) Left. Macroscopic view. Tm is the bulk melting temperature. The water between the bottom surface of the ice and the dotted line is supercooled. The gradient in chemical potential pulls up the supercooled water which freezes at the bottom of the ice lens. Simultaneously, the existing ice lens is lifted up. Right. Microscopic view of the soil/lens interface. The interface consists of alternation of pores (between two particles) and premelted films (between a particle and the ice lens).

In soils, freezing causes an upward displacement of the ground surface, a phenomenon called frost heave. Frost heave is mainly caused by the formation of layers of bulk ice within the soil, called ice lenses (Figure 3.1). Qualitatively, because

the ice is thermodynamically more stable than supercooled water, there is a chemical potential gradient which creates a thermodynamic driving force. The water is drawn from the groundwater to the frozen regions, causing the growth of the ice lens and the elevation of the surface of the soil. Although they create beautiful patterns in the soil [8], the frost heaves also damage infrastructures like buildings, roads, pipelines. Costs needed to repair those damage have been estimated to 2 billion dollars in the US [9]. More precisely, the water at the interface equilibrates with the macroscopic ice and its pressure decreases (cf background). Because the water located deeper in the soil is at higher pressure, a pressure gradient appears which pushes the liquid into the ice. At the interface, the liquid coming from the soil freezes onto the macroscopic ice which moves upwards. This phenomenon has been clearly demonstrated by Ozawa and Vignes [10,11]. However, the path of the flow at the interface is unknown. Figure 3.1 shows a hypothetical scenario where liquid travels through the premelted layers at the interface. The transport of water through those thin films would slow down the kinetic of frost heave [7].

3.2 Cold hardiness in plants

Frost damage to plants results in huge loss of profits [13]. For example, spring frost causes crop losses that threatens the sustainability of fruit producers. In the production of wine, the losses caused by a single event in January 2004 in the Finger Lakes region were estimated at 47.2 million dollars. Cold hardiness is the ability of plants to survive subfreezing temperatures [14]. It is a very complex trait that is still poorly understood. However, it is clear that the physical consequences of the coexistence of ice and liquid in plant tissues are crucial.

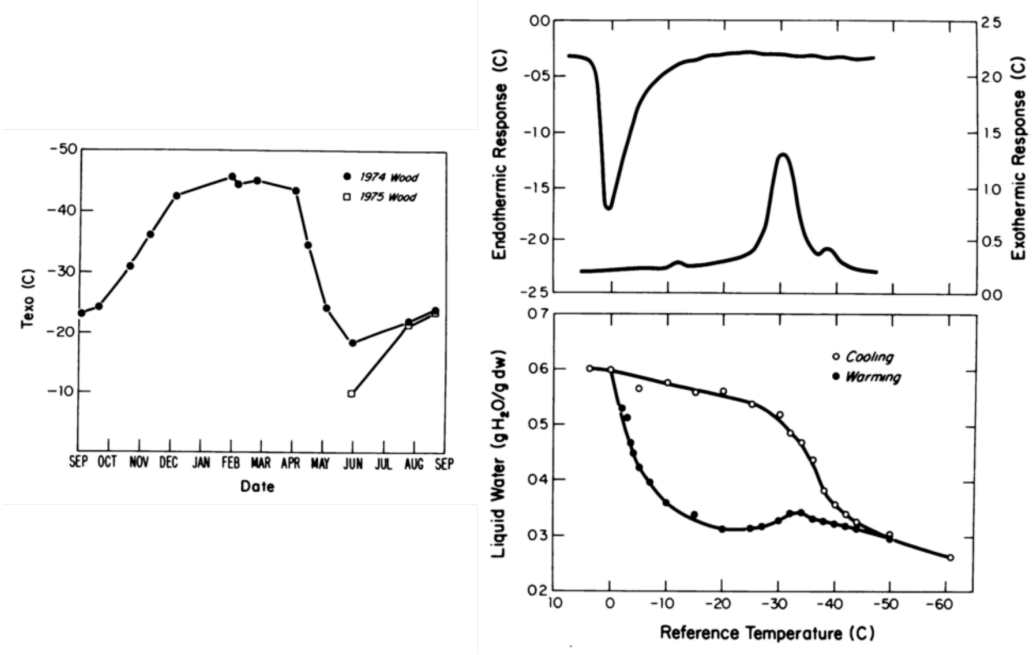

Figure 3.2: Supercooling in xylem of shagbark hickory tree (Reproduced from [12]). Left. Evolution of the LTE measured by DTA in the course of a year. Upper right. Typical DTA scan. Lower right. Typical NMR freezing and thawing curve. Vertical axis shows the mass proportion of liquid water to dry sample.

Plant cells die if they freeze. Plants have developed strategies to prevent cells from freezing. When a plant tissue is cooled to subfreezing temperature, the extracellular water freezes first, while the water inside the cells remains liquid. The cell wall plays a crucial role to isolate the intracellular water from the ice outside [15]. From there, plants strategies can be classified in two categories:

3.2.1 Freeze tolerance

Because of the difference in chemical potential, intracellular water is drawn out of the cell. As a result, the protoplasm shrinks and the solute concentration increases in the cytosol [16]. The freezing point of the solution therefore decreases until it becomes equal to the temperature of the tissue. At this point, desiccation stops as

the cytosol is in equilibrium with the ice. Because the cytosol is not supercooled anymore, the cells are protected from freezing. The downside of this strategy is that high solute concentration causes damage to membranes and might require extra chemical protection from the cell.

3.2.2 Freeze avoidance

In that case, there is no rapid transfer of water from the cell to the apoplast. Thus the solute concentration cannot increase and the cells are supercooled. The causes of freezing of these supercooled cells are poorly understood. For example, freezing could happen by homogeneous nucleation, heterogeneous cavitation, seeding of ice, failure of ice barriers or of antifreeze proteins. The temperature threshold at which intracellular freezing occurs (referred to as Low Temperature Exotherm) has been extensively studied. It has been experimentally measured by various methods such as DTA (differential thermal analysis), DSC (differential scanning calorimetry) and NMR (Figure 3.2). The LTE shows seasonal variations as the plants gradually increase their cold hardiness in late fall and winter (acclimation) and lose hardiness in the spring (deacclimation). Also, the geographical distribution of the LTE correlates with the minimum local temperature. Thus, some species are able to supercool very close to the temperature of homogeneous nucleation, like shagbark hickory trees in Minnesota [12]. Anatomically, plants that supercool need rigid walls with low permeability. If the walls are rigid, it is expected that supercooled water equilibrates with ice by lowering its pressure. The predicted pressure (see Chapter 4) for pure water at equilibrium at the homogeneous nucleation limit($-38\,^{\circ}\mathrm{C}$) is $\sim -400\,\mathrm{bar}$. If this is true, it would mean that cells have extremely high resistance to cavitation, in addition to amazing resistance to freezing. Researchers

have suggested that freezing avoidance plants might save energy because they don't need to actively counteract the effects of desiccation and have more energy available to grow fast in the spring [15]. However, little is known about the biological mechanism that regulate acclimation or the physical phenomenon responsible for intracellular freezing.

3.3 Porous solids

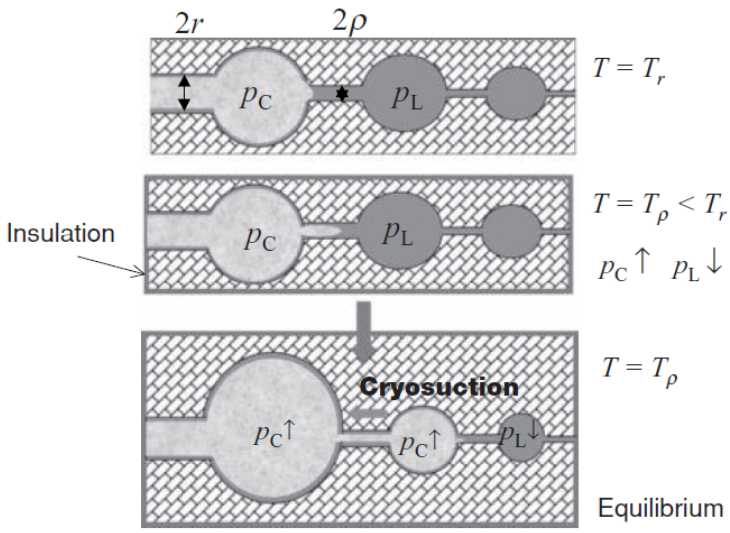

Figure 3.3: Crysuction and cryogenic swelling (Reproduced from [17]). The voids are connected by narrow channels. T_r (resp. T_ρ) is the Gibbs-Thomson temperature for a channel of radius r (resp. ρ). Top. The porous solid is at equilibrium at temperature T_r. The ice in the pore is at pressure P_C and the liquid at pressure P_L. P_C and P_L are such that $\mu_C(P_C, T_r) = \mu_L(P_L, T_r)$. Middle. The temperature is decreased to T_ρ. The liquid freezes in the channel of radius ρ and the solid propagates to the next void. Bottom. Consequently, liquid is sucked in the frozen pore to restore equilibrium. The initial difference in chemical potential following the drop in temperature is balanced by an increase in P_C (which causes swelling) and a decrease in P_L.

A porous solid can be seen as a networks of interconnected voids called pores. The pore size distribution may be spread over several orders of magnitude. Be-

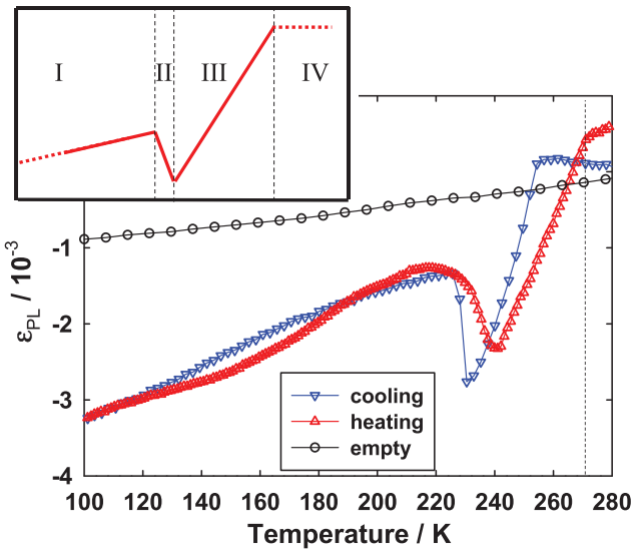

Figure 3.4: Deformation of a water saturated porous media in equilibrium with bulk ice (reproduced from [4]). Pore lattice strain versus temperature. The sample is MCM-41 with measured pore size 4.4 nm. The dotted line shows the bulk melting point. The black circles show the deformation of an the empty sample. The blue (resp. red) triangles show the deformation of the sample during cooling (resp. heating). The inset shows four temperature regions. IV $T \geq T_0$. III $T_0 \geq T \geq Tf$, the liquid is supercooled and supposedly in equilibrium with ice. In this region, the strain varies approximately linearly with temperature. II Phase change. I Medium completely frozen, deformation of the matrix by thermal expansion of ice.

cause of confinement, ice nucleated in big pores cannot enter small pores until the temperature is low enough. As a result, mass transfer between supercooled water and ice takes place to homogenize the chemical potential in the porous solid. This phenomenon has dramatic and non intuitive consequences on the solid matrix. For example, although it has been thought for a long time that frost damage to roads and buildings was caused by the expansion of water upon freezing, experiments have shown that similar deformations are caused by benzene that contract upon freezing. Let's consider two extreme cases, represented in Figure 3.3.

(1) Ice has a limited volume (confined in a pore for example) and connected to a reservoir of water at constant pressure. Because ice has initially a lower chemical

potential, liquid will be drawn to the ice. The supply of matter will increase the pressure of ice until its chemical potential becomes equal to that of the liquid. The increase in pressure may cause failure of the material. This explains the origin of frost damage. Besides, it is clear that this reasoning applies equally to liquid that either expand or contract upon freezing.

(2) Liquid is confined in a pore and connected to a reservoir of ice at constant pressure. This time, the supply of matter from liquid to ice will cause a decrease in pressure of the liquid, until its chemical potential becomes equal to that of ice. The liquid experiences negative pressure, which causes deformation of the material and can also cause cracks and failure [18].

Erko and al. [4] measured the deformation of a water saturated porous media in equilibrium with bulk ice as a function of temperature (Figure 3.4). They observed that the porous sample linearly shrank when temperature was decreased, which is consistent as the pressure of the liquid in the pores should decrease. Quantitatively, they used the theoretical linear temperature dependence of the pressure (see theory) to extract the expected "pore load modulus" $M_{PL} = \frac{P}{\epsilon_{PL}}$ from their data. They found that their value systematically differed from the experimental value obtained with liquid/vapor equilibrium by 15%. Although these measurements are undirect, they are rather consistent with generalized Clapeyron equation. This study is probably the work which is the most similar to ours.

CHAPTER 4

STUDY ON WATER

In this chapter, we present our work on the pressure of supercooled liquid in equilibrium with ice. We start by a theoretical derivation where we obtain an analytical expression for the pressure. We also give a detailed presentation of the microtensiometer. We explain how to fabricate, calibrate and package the sensors. We then present and discuss our experimental microtensiometers. We have been able to directly measure the pressure and temperature of a macroscopic volume of supercooled liquid in equilibrium with ice. The data is in quantitative agreement with the theory. We also report and discuss dynamic transient effects.

4.1 Theory

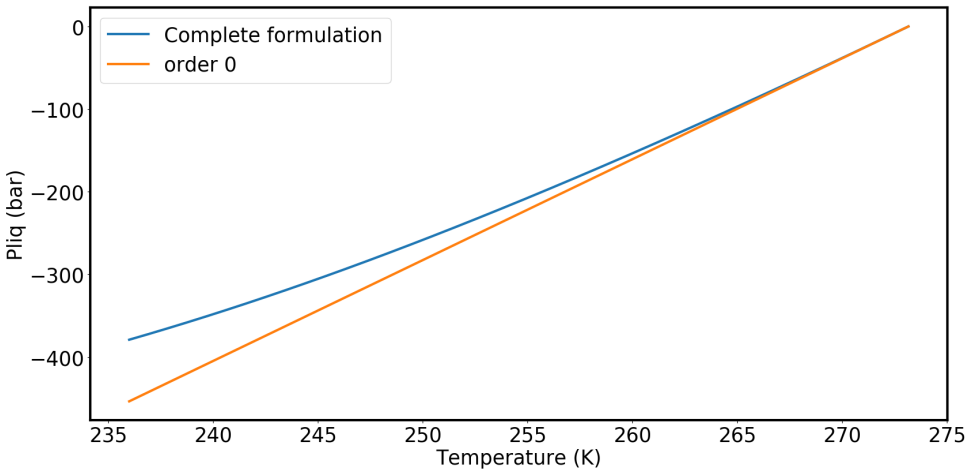

Figure 4.1: Theoretical pressure in supercooled water in equilibrium with ice. The pressure of ice is fixed at P_t. The blue line is the more complete expression including the correction term with the heat capacities and orange line is the linearized zero-order expression.

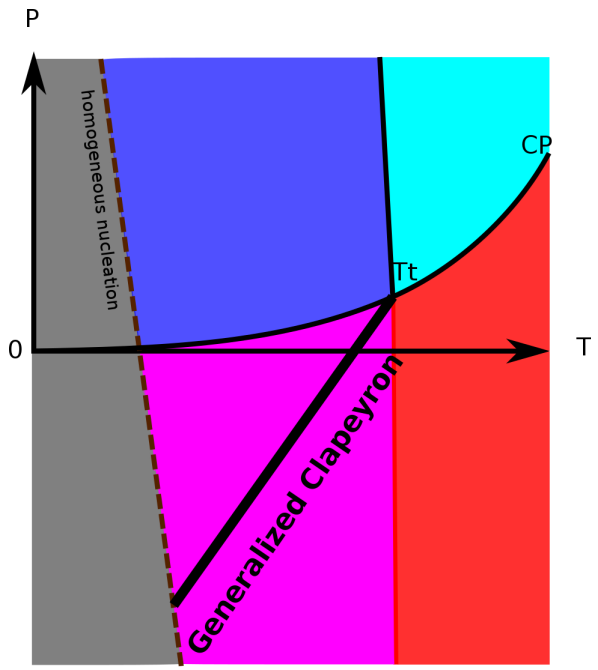

Figure 4.2: Extended phase diagram of water. Top. The thin black lines are the binodal lines which describe stable equilibrium. The thick black line represents the pressure in liquid water in equilibrium with ice, as predicted by the generalized Clapeyron equation, assuming that pressure of the ice is P_t. The colored domains represent the different state of liquid water. Light blue is stable domain, red is superheated (metastable relative to boiling), dark blue is supercooled (metastable relative to freezing) and purple is doubly metastable (metastable relative to both boiling and freezing). The dashed light blue line represents the homogeneous nucleation limit. Beyond this line, it is not possible to experimentally study liquid water. The gray domain is therefore called "No Man's Land".

We now expand eq. (2.9) to extract an explicit relation between P_s, P_l and T. Taking the Triple point T_t as our reference state, we can write the general expression for the chemical potentials:

$$\mu_s(P_s, T) = \mu_s(P_t, T_t) + \int_{P_t}^{P_s} v_s(P, T)dP - \int_{T_t}^{T} s_s(P_t, T)dT \tag{4.1}$$

$$\mu_l(P_l, T) = \mu_l(P_t, T_t) + \int_{P_t}^{P_l} v_l(P, T)dP - \int_{T_t}^{T} s_l(P_t, T)dT \tag{4.2}$$

By definition,

$$\mu_s(P_t, T_t) = \mu_l(P_t, T_t) \tag{4.3}$$

Eq. (2.9) leads to:

$$\int_{P_t}^{P_s} v_s(P,T)dP - \int_{P_t}^{P_l} v_l(P,T)dP = \int_{T_t}^{T} (s_s(P_t,T) - s_l(P_t,T))dT \tag{4.4}$$

And

$$s_s(P_t,T) - s_l(P_t,T) = \int_{Tt}^{T} \frac{c_s(Pt,T) - c_l(Pt,T)}{T} dT + s_s(Pt,Tt) - s_l(Pt,Tt) \tag{4.5}$$

By definition

$$s_s(Pt,Tt) - s_l(Pt,Tt) = -\frac{l_{f_t}}{T_t} \tag{4.6}$$

Therefore,

$$\int_{P_t}^{P_s} v_s(P,T)dP - \int_{P_t}^{P_l} v_l(P,T)dP = \int_{T_t}^{T}\int_{Tt}^{T} \frac{c_s(Pt,T) - c_l(Pt,T)}{T} dTdT + \frac{l_{f_t}}{T_t}(T_t - T) \tag{4.7}$$

Equation (4.7) is exact. We can further make the assumption that the molar volumes are independent of the pressure (the corrective term is negligible compared to all the other terms). We get:

$$v_s(T)(P_s - P_t) - v_l(T)(P_l - P_t) \approx \int_{T_t}^{T} \int_{Tt}^{T} \frac{c_s(Pt,T) - c_l(Pt,T)}{T} dT dT + \frac{l_{f_t}}{T_t}(T_t - T) \tag{4.8}$$

Finally, we can extract P_l as a function of P_s and the temperature.

$$P_l - P_t \approx \frac{v_s(T)}{v_l(T)}(P_s - P_t) - \frac{l_{f_t}}{v_l(T)T_t}(T_t - T) + \frac{1}{v_l(T)} \int_{T_t}^{T} \int_{Tt}^{T} \frac{c_l(Pt,T) - c_s(Pt,T)}{T} dT dT \tag{4.9}$$

The true equilibrium diagram $P_l(P_s, T)$ is a 3D plot, but it can be easily represented as a 2D plot without loss of generality because P_l depends linearly on P_s. The plot on Figure 4.1 shows the prediction of $P_l(T)$ with $P_s = P_t$. At moderate supercooling, the dependence is almost linear and close to order 0:

$$\frac{l_{f_t}}{v_l(T_t)T_t} = 12.2 bar/K \tag{4.10}$$

Up to this point, no assumptions have been made on the geometry of the liquid-ice interface. The conclusions are only based on chemical equilibrium between two bulk phases and they are general.

4.2 Materials and Methods

4.2.1 Description and working principle of microtensiometer

The microtensiometer is described on Figure 4.3. The microtensiometer can be seen as a single macroscopic void (the cavity) connected to narrow channels (the

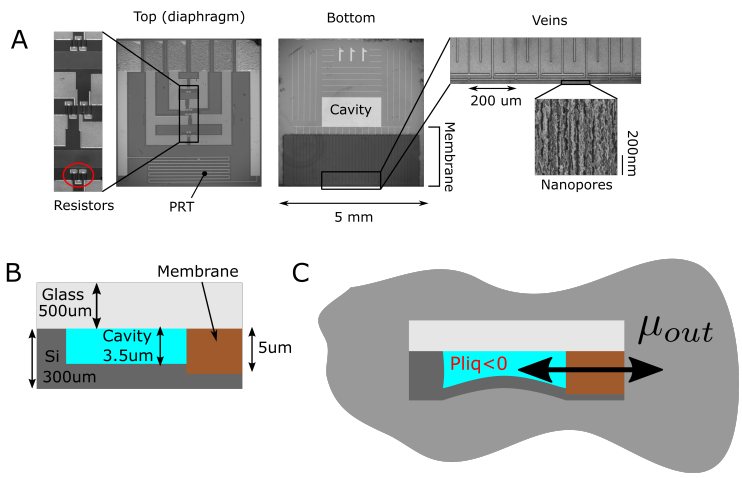

Figure 4.3: Description and working principle of microtensiometer. A. Photographs of the microtensiometer. The thermometer (PRT) and the strain gauge are patterned on the top side. One of the four resistors of the gauge is circled in red in the expanded view. The bottom view shows the cavity and the membrane. The membrane is composed of nano-porous silicon (dark area) coupled to microscopic channels called veins (expanded view). B. Schematic representing side view of the microtensiometer (not to scale). C. Working principle of the microtensiometer. The sketch shows a microtensiometer immersed in an environment (for example, water vapor, ice, aqueous solution). The chemical potential of water inside the environment is fixed at μ_{out}.

membrane). The cavity is macroscopic (the smallest length is 3 µm long) so that the liquid inside behaves like the bulk. The wall of the cavity has a strain gauge and a platinum wire attached to it, which allow to measure the pressure and the temperature of the liquid. When the microtensiometer is immersed in an environment that contains water at a fixed chemical potential of μ_{out} different from $\mu_w(Patm, T)$, mass flux arises to balance the chemical potentials. For example, if $\mu_{out} < \mu_w(Patm)$ (like in Figure 4.3), water is transported from the cavity to the environment until the pressure reaches a new value P_l such that $\mu_w(P_l, T) = \mu out$. This leads to:

$$P_l \approx Patm + \frac{\mu_{out} - \mu_w(Patm, T)}{v_l} \tag{4.11}$$

4.2.2 Fabrication, calibration and packaging

The microtensiometer was originally developped in the Stroock group by Pagay and Santiago [19].

Fabrication of tensiometers

Substrates

Double-side polished silicon wafers (4" diameter, 300 µm thickness, p-type doping, 1–10 Ω cm resistivity range and <111> orientation). Borofloat 33 glass wafer, double-side polished (4" diameter, 500 µm thickness, prime grade). Reagents: hydrofluoric acid (49% w/w, in H_2O; Sigma-Aldrich), ethanol (95% v/v; Sigma-Aldrich).

Power supply for electrochemical etching: Hewlett Packard DC power supply (Model 6634B). Major microfabrication tools used in the cleanroom were: oxide and thin-film deposition furnaces, photolithographic tools (resist spinner, contact aligner, wafer developer), wet etching reagents, dry etching tools (RF plasma etchers, oxygen plasma asher), PECVD thin film deposition, evaporator (thin film metal deposition), high-temperature annealing tool, substrate bonder, and wafer dicing saw. Process characterization tools included profilometer, Filmmetrics thin film thickness analyzer.

Process flow

I fabricated a new batch of sensors at the CNF which I used for my experiments. Briefly, a layer ~ 1 µm thick of SiO_2 was grown by thermal oxidation in a furnace at 1000 °C for electrical insulation. Then doped p+ polysilicon was deposited over

the SiO_2 in a LPCVD furnace at 620 °C to a thickness of $\sim$ 900 nm for the resistors. On the front side of the wafer, the resistors were patterned by photolithography and plasma etching. On the backside of the wafer, the cavity and veins were patterned and etched to a depth of 3 µm using plasma etching. The membrane of nanoporous silicon was patterned and etched using a custom-built electrochemical etch cell. Electrochemical etching was done under at a density of 20 $mAcm^{-2}$ for 5 minutes, resulting in a $\sim$ 5 µm thick layer of porous silicon. The average pore size was $\sim$ 2 nm. The porous silicon was then annealed at 700 °C for 30 s in an O_2 environment. The sililcon wafers were then anodically bonded to glass at 400 °C and 1200 V. Then, metal was evaporated on the frontside to form the connections to the resistors, the PRT and the pads. The evaporated metal consisted in a stack of Titanium/Platinum/Titanium respectively 15/200/15 nm. Finally, the electronics on the frontside was protected by depositing a passivation layer. Individual chips were released from the wafer by dicing with a wafer saw.

Packaging

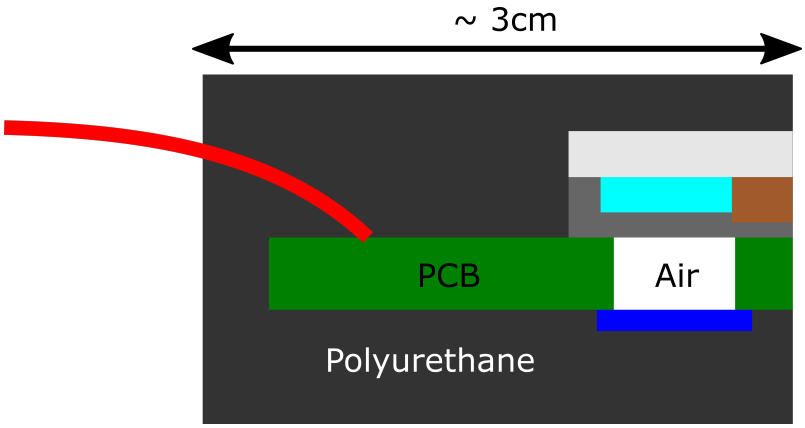

Figure 4.4: Packaging of a sensor. The hole in the PCB was sealed by a adhesive material (blue rectangle)

I then packaged each chip into a usable format (Figure 4.4). The chip was

soldered to a custom-designed PCB. The pads on the PCB were first wet with solder. The chip was stacked on the PCB and aligned before heating on a hot plate to melt the solder and wet the chip's pads. The stack was finally cooled down to finish the connection. Then electrical wires were soldered to the PCB. The device was further encapsulated in polyurethane so that only the tip of the membrane was exposed. Precautions were taken to leave a layer of air on top of the diaphragm to decouple the sensor from any exterior mechanical stress.

Calibration

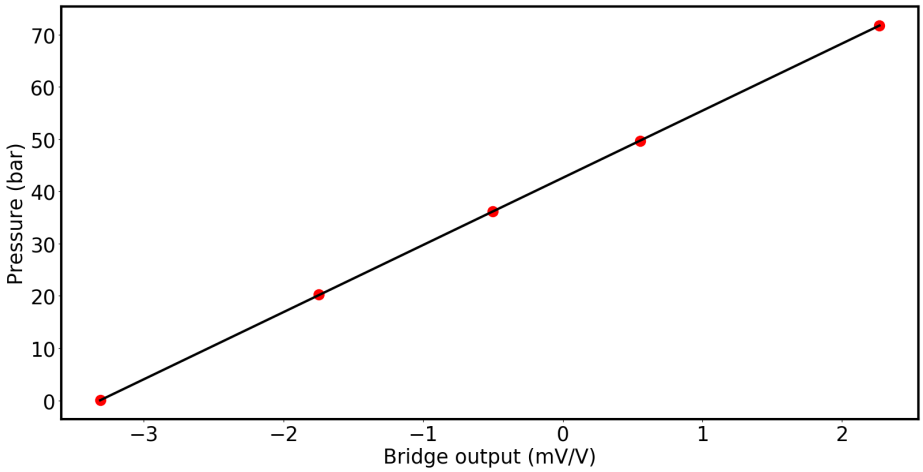

Figure 4.5: Pressure calibration

To calibrate the strain gauge (Figure 4.5), the sensor was put in a chamber connected to a nitrogen gas cylinder with a pressure valve. The positive pressure of the gas was measured by a commercial sensor. Prior to calibration, the membrane was sealed with parafilm and latex to avoid entry of air. The pressure was varied by steps and the output of the Wheatstone bridge was measured. The PRT was calibrated against a commercial PRT (Figure 4.6). Both thermometers were immersed in a water bath whose temperature was varied by steps. Even without

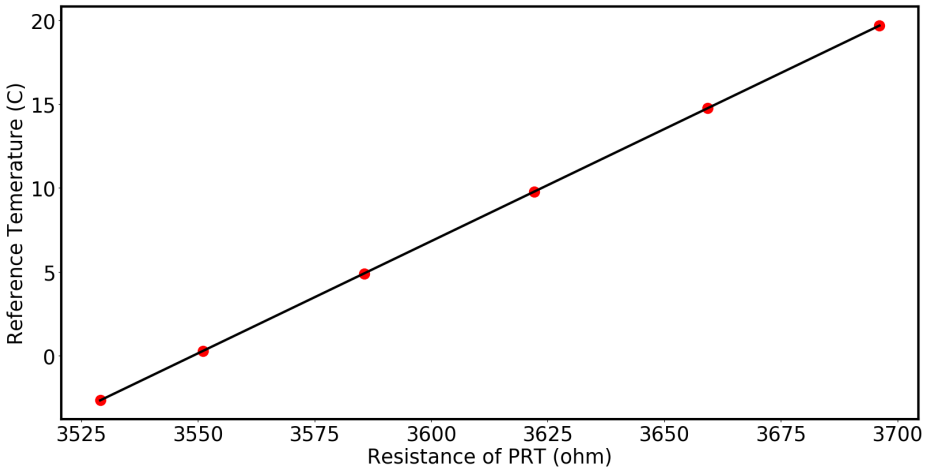

Figure 4.6: Temperature calibration

any deformation of the diaphragm, the output of the bridge was not exactly zero (see Figure 4.5) because the resistors were not perfectly trimmed. We observed that this offset varied linearly with temperature. This variation was taken into account to correct the bridge signal during pressure calibration and experiments.

4.2.3 Experiment

The microtensiometer was first filled with water under high pressure ($\sim 35\,\text{bar}$) for at least 6 hours. This was enough to dissolve the air initially present in the cavity. The full sensor was then immersed in a plastic container filled with water. The container itself was partially immersed in a temperature controlled bath. The bath temperature was then set to about $\sim 1\,°\text{C}$. Because water supercooled easily at this temperature, freezing was initiated by contacting the water with a piece of ice. Subsequently, the ice phase slowly grew from the edge of the container to the center until all the water had frozen. At this point, the sensor was fully embedded in ice. The bath temperature was varied by steps. The temperature

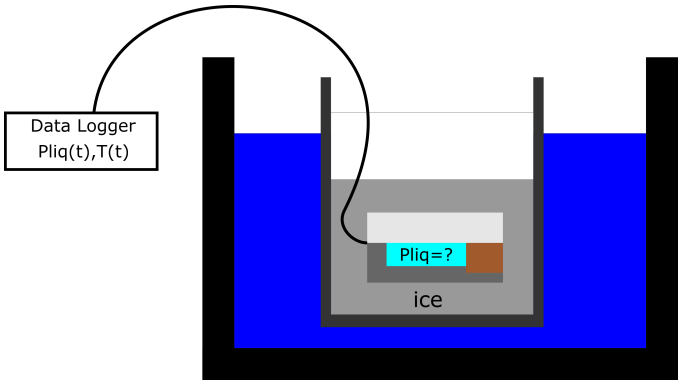

Figure 4.7: Experimental setup. The plastic container (dark gray) was partially immersed in the bath coolant (dark blue). The temperature of the coolant was controlled by the bath (black). Inside the plastic container, the microtensiometer was fully embedded in ice. The pressure of the liquid and the temperature were recorded by the data logger.

of the microtensiometer was measured by the PRT and the pressure of the liquid inside the cavity was recorded by the strain gauge. The measurements were done with a commercial data logger CR6 from Campbell Scientific. The excitation voltage of the bridge was 500 mV and the PRT was excited with a current of 200 μA.

4.3 Results and discussion

4.3.1 Thermodynamic equilibrium

Upon a change in temperature, the pressure was continously monitored and was observed to stabilize. When the pressure was stable, the system was assumed to be in equilibrium. In this section, we report our measurements of the pressure at equilibrium for different temperatures. Figure 4.8A shows a typical experimental curve. As expected, the supercooled liquid decreased its pressure to remain in

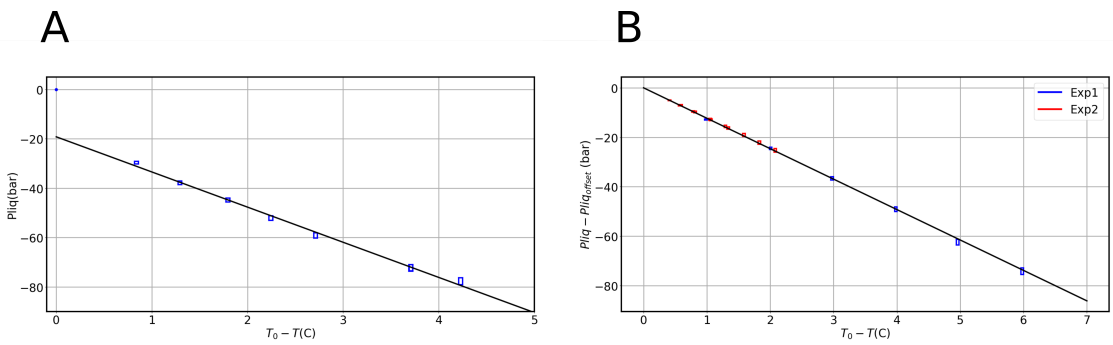

Figure 4.8: Pressure in the liquid Versus Temperature at equilibrium. A. Pressure in water in equilibrium with ice for a typical experiment. The size of the box corresponds to experimental uncertainties. The measurement (0 bar,0 C) is exact. The black line was obtained by a linear fit the data excluding the point (0 bar,0 C) B. Corrected pressure in water in equilibrium with ice for two experiments. The black line is a linear fit of all the data, with the intercept forced at 0 bar.

equilibrium with ice. Besides, the pressure varied approximately linearly with temperature. However, it can be seen that the line has a non-zero intercept. The possible reasons for this offset are discussed later. For each experiment, we fitted the linear portion of the data with the least square method to obtain the value of the offset. On Figure 4.8B, we combined the results of two experiments where the pressures have been corrected by subtracting the value of the offset. The data was then fitted by a linear model with the intercept forced at 0 bar. The experimental value of the slope of -12.3 ± 0.8 barK^{-1} is in excellent agreement with the theoretical slope predicted by the Generalized Clapeyron equation. To the best of our knowledge, our work is the first to provide a direct confirmation of the generalized Clapeyron equation at negative pressure. We note that Erko [4] measured the deformation of a water saturated porous sample in equilibrium with bulk ice by X-ray diffraction. Even though their results agreed qualitatively with the generalized Clapeyron equation, they reported systematic inconsitensies that they attributed to confinement of the water. Whereas in our experiment, we have a macroscopic volume of water in equilibrium with ice.

Although the local pressure of the ice at the membrane could not be measured, the results suggests that it remained approximately constant during the experiment (or at least negligible compared to $-12.2\,\mathrm{bar K}^{-1}$).

The offset varied across experiments –even with the same sensor–and was found to be either positive or negative. It is possible that the freezing of the water in the container is responsible for the offset. For example, if ice locally experiences a compressive stress at the interface, it is clear from the generalized Clapeyron equation that the pressure of the liquid will be shifted to higher values, thus creating a positive offset in the curve. Moreover, despite of the precautions taken to isolate the sensor, it is possible that the strain gauge was still mechanically coupled to the outside. If the ice embedding the sensor pushed on the strain gauge, it would lead to an overestimation of the magnitude of the pressure and generate a negative offset. However, these hypotheses could not be tested.

4.3.2 Kinetics

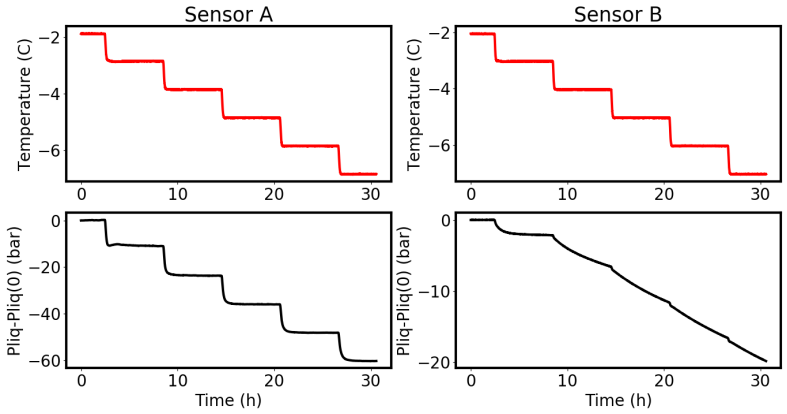

Figure 4.9: Pressure transient. Transient evolution of pressure upon a step change in temperature for two different sensors.

As explained above, when temperature is decreased, the supercooled liquid

phase decreases its pressure to restore equilibrium. In this process, a small amount of liquid is transported through the membrane from the cavity to the ice phase where it freezes. Conversely, when temperature is increased, a small amount of ice melts and is transported inside the cavity through the membrane to increase the pressure. We can study the dynamics of these transient evolutions. It is possible to compare these transients with a reference characteristic time which we call the "intrinsic transient" of the microtensiometer $\tau_{intrinsic}$. When a microtensiometer initially under tension (negative pressure) is immerged in pure water, the pressure relaxes exponentially with a characteristic time that only depends on intrinsic properties of the microtensiometer (hydraulic resistance of the membrane and mechanical properties of the strain gauge). On Figure 4.9, it can be seen that the transients exhibit two dramatically different behaviors. (1) Upon a step change in temperature, the pressure reaches its new equilibrium value with a characteristic time $\tau \sim \tau_{intrinsic}$. This is the case of sensor A. The temperature transient does slightly influence the dynamic but is not limiting. (2) The pressure reaches its new equilibrium value with a characteristic time $\tau \gg \tau_{intrinsic}$. In some experiments the transients transitioned from behavior (1) to behavior (2) as the temperature was continuously decreased. An example of this behavior is shown with sensor B.

Behavior (1) suggests that presence of macroscopic ice at the mouth of the pore did not affect the transport of water significantly. This result contrasts with previous works [20] which reported that transport can be considerably slowed down by the presence of the interface. It has been suggested that at the interface, the water circulates through premelted thin films along the surface of ice [3], creating an additional hydraulic resistance $R_{interface}$ in series with the porous matrix R_{matrix}. We estimated that for a microtensiometer, R_{matrix} is worth 10^{20} Pam^{-3}s. Behavior (1) suggests that $R_{interface} \leq R_{matrix}$. Style and Peppin [7] derived a analytical

expression for $R_{interface}$ based on lubrication theory. Based on their calculations, we can estimate the order of magnitude of R_{matrix}

$$R_{interface} \sim \frac{\mu r^2}{d^3 S} \tag{4.12}$$

Where r is the radius of the pore, μ the viscosity of water, d the thickness of the liquid-like film and S the surface of the interface. We find that $R_{interface} \sim 10^{15}$ $\mathrm{Pam^{-3}s}$, which confirms our insights.

However, behavior (2) seems to challenge this interpretation and we have no clear explanation for why this is happening. We propose the following reasoning. To accomodate the water coming from the cavity, the ice has to deform. As a result, it might experience compressive stress which would increase the chemical potential of the ice. Consequently, the thermodynamic driving force would be transiently decreased, slowing down the equilibration process. This interpretation does not necessarily contradict the conclusions of behavior (1).

4.3.3 Failure of the microtensiometer

At temperature higher than the melting point, the mode of failure of the microtensiometer is cavitation: the spontaneous formation of vapor relaxes the state of negative pressure. The typical pressure at which cavitation occurs is $-100\,\mathrm{bar}$. This value is much smaller than the prediction of the Classical Nulceation Theory ($\sim -100\,\mathrm{MPa}$), suggesting that cavitation occurs heterogeneously. In our experiment, the water is in the doubly metastable regime. Therefore, failure can be caused by either nucleation of vapor or nucleation of ice. Failure may also be caused by the freezing of the water confined inside the membrane. From the Gibbs-Thomson equation (**??**), this occurs at $-25\,^{\circ}\mathrm{C}$ assuming that water perfectly wets the wall

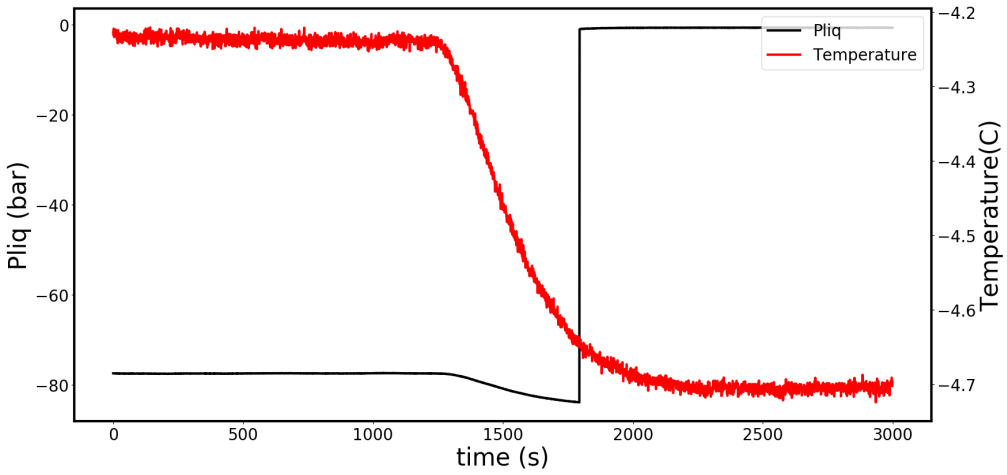

Figure 4.10: Failure of the microtensiometer. Typical evolution at failure. At failure, the pressure was −84 bar and temperature −4.65 °C.

in ice. At −25 °C, the liquid would have a pressure of about −300 bar which is much lower than the typical cavitation pressure. Therefore we did not expect to observe the freezing of the confined water. Figure 4.10 shows what typically happens at failure. The pressure suddenly rose back to 0 bar at a pressure close to the typical cavitation limit. Besides, the corresponding temperature was high enough so that ice nucleation was not expected. This suggests that vapor nucleated first in supercooled water.

CHAPTER 5

STUDY ON ACETIC ACID

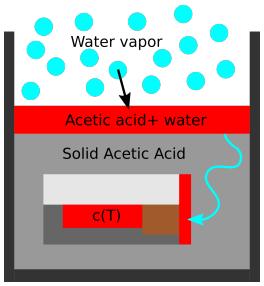

Figure 5.1: Experiment with acetic acid. Contamination by water (light blue) and formation of a mixture of water and acetic acid (red) in equilibrium with the solid acetic acid (gray).

The experiment described in 4.2.3 was repeated with acetic acid (Sigma Aldrich 100% glacial). The generalized Clapeyron equation predicts a slope of $-6.6\,\mathrm{barK}^{-1}$. The same protocol was applied. However, we observed that the pressure did not vary. We think that this might come from contamination of water from the atmosphere that condensed and diffused through the solid phase (see Figure 5.1). The mixture of water and acetic acid would be in equilibrium with the pure solid, with a concentration imposed by the temperature. Mathematically, the equilibrium would be governed by the following equation:

$$\mu_l(P_{atm}, T, c) = \mu_s(P_{atm}, T) \tag{5.1}$$

In the diffusion process, the formation of thin film of solution around the microtensiometer would pin the equilibrium pressure at atmospheric. The mixture in the cavity would simply change its concentration by diffusion of water. In other words, it would now be the concentration of solute and not the pressure that adapts to balance the chemical potentials. If the concentration is low enough, we can write:

$$\mu_l(P_{atm}, T, c) \approx \mu_l(P_{atm}, T) - RTc \tag{5.2}$$

and

$$c \approx \frac{\mu_l(P_{atm}, T) - \mu_s(P_{atm}, T)}{RT} \tag{5.3}$$

This result suggests that even small contamination of the solvent might dramatically affect the nature of equilibrium. Indeed, it would no longer be an equilibrium between solid and supercooled liquid but simply between solid and solution. To gain more insights, it would be interesting to repeat the experiment described in section 4.2.3 with aqueous solutions instead of pure water. This phenomena might play an important role in frost heaves because the water contained in the soil is not pure.

CHAPTER 6

TRANSPORT OF SUPERCOOLED LIQUID INTO THE FROZEN PHASE

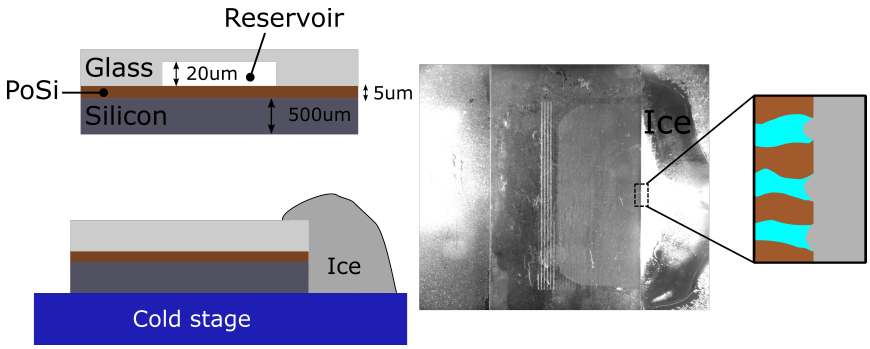

Figure 6.1: Study of the cryosuction dynamics. Experimental setup. Upper left. Schematic of sample. The porous silicon is coupled to a reservoir of water that pins the pressure at the back edge of the porous matrix and allows to track the flux. Lower right. Sketch of experiment. The water saturated sample is set on a temperature controlled stage. The front edge of the sample is in contact with bulk ice. Right. Photograph of experiment. The sketch on the right of the photograph shows an expanded view of the interface.

If the chemical potential is not uniform throughout the media, mass transport occurs to restore equilibrium. It is crucial to thoroughly study the kinetic of this process for several reasons. On the fundamental level, this would shed light on the nature of the transport happening at the interface and help understand the results obtained in section 4.3.2. It is also of practical importance because the damage done by frost heave or cryogenic swelling depends directly on the rate of mass transfer.

6.1 Materials and Methods

The experiment described in Figure 6.1 is designed to study the kinetic of the cryosuction process. We used microfluidic devices combining microfluidic channels

and nano-porous media (see [21] for details) to measure the thermodynamically driven flux of supercooled water into ice. As explained in [21], the resistance of the porous media R_{sample} can be experimentally measured by equilibrating the saturated sample with sub-saturated water vapor and measuring the corresponding flux. After measuring the resistance, we equilibrated the sample with ice at different temperatures and measured the flux $\frac{\mathrm{d}V}{\mathrm{d}t}$. We then computed the pressure in the liquid at the interface P_l and compared it to the prediction of the generalized Clapeyron equation.

$$P_l = R_{sample}\frac{\mathrm{d}V}{\mathrm{d}t} \tag{6.1}$$

6.2 Results and discussion

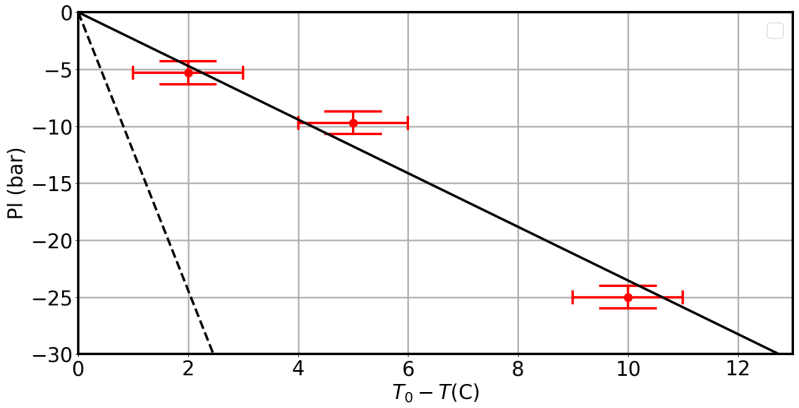

Figure 6.2: Cryosuction dynamics. P_l is the pressure computed from equation (6.1). The black plain line is a linear fit of the data. The black dashed line has a slope of $-12.2\,\mathrm{barK}^{-1}$

.

We expect that the liquid at the interface equilibrates with the ice, therefore its pressure P_l should follow the generalized Clapeyron equation. Figure 6.1 shows

our experimental results. As expected, the pressure in the liquid decreases with increasing supercooling. However, the linear fit yields a slope of -2 ± 1 barK^{-1}, which is about five times lower in magnitude than the prediction of the generalized Clapeyron equation. This indicates that kinetics of transport is slower in the presence of ice. As in section 4.3.2, we expect the interfacial resistance to be negligible compared to that of the porous matrix. Therefore, our result is similar to behavior (2) observed in tensiometers (see 4.3.2). We suspect that as water is sucked in the ice phase, the ice deforms and experiences compressive stress. As a result, the pressure in the ice at the interface increases, which decreases the thermodynamic driving force by rising the pressure in the liquid at the interface. Interestingly, the flow reaches a steady-state, which means that the deformation of ice is not purely elastic (otherwise, the pressure of the ice would keep increasing and the flow would stop when the chemical potentials are balanced). Instead, we suspect that ice experiences plastic deformation. To further test these hypotheses, it would be interesting to monitor the pressure of the ice at the interface.

CHAPTER 7

FUTURE WORK

7.1 Study of cryogenic swelling

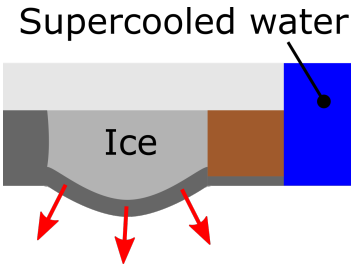

Figure 7.1: Study of cryogenic swelling with a microtensiometer. The microtensiometer is filled with ice and equilibrated with a reservoir of supercooled liquid at constant pressure.

As described in section 3.3, cryogenic swelling is the process by which the pressure of a crystal increases to balance the chemical potentials of solid and supercooled water. The pressure rises because supercooled water is forced into the frozen pore and subsequently freezes. So far, this process has never been directly observed. With the microtensiometer, we could make a direct observation of this phenomenon. We propose an experiment where the cavity would be filled with ice and the sensor immersed in supercooled water at atmospheric pressure. Besides, we could characterize the kinetics of the equilibrium, notably how the pressure is transmitted through the crystal. Indeed, as Scherer states in [18] :"a process of dissolution and reprecipitation will proceed until [the pressure] is constant within the crystal".

7.2 Study on doubly metastable liquid

The doubly metastable regime still remains largely unexplored [22]. With our microtensiometer, we can bring a liquid into the doubly metastable regime and have a direct measurement of its pressure and temperature. In addition, we can optically observe the liquid. This would enable us to gain insights on how doubly metastable liquids relax to equilibrium [23]. In particular we would better understand how cavitation catalyses freezing. This is of practical interest for industrial processes which uses insonation of solidifying liquid and solutions to produce small and uniform crystals [24].

CHAPTER 8

CONCLUSION

We have used a homemade MEMS device called microtensiometer to measure the pressure in a macroscopic volume of supercooled water in equilibrium with bulk ice. The pressure was found to follow the generalized Clapeyron equation. We also reported two dramatically different dynamics of equilibration with several orders of magnitude of difference in the equilibration transients. This observation has motivated a more careful study of the kinetics of cryosuction. The data indicated that the transport of water into the frozen phase was slowed down by the presence of the ice. We suggested that, in order to accommodate the incoming water, the ice experiences compressive stress causing plastic deformation and decreases the thermodynamic driving force. We repeated the experiment with water on acetic acid. The absence of pressure variation was attributed to contamination of the solid by water causing the formation of a binary mixture in equilibrium with the solid phase. Further experiments with aqueous solutions should provide more insights to explain this result.

BIBLIOGRAPHY

[1] Gerhard H. Findenegg, Susanne J??hnert, Dilek Akcakayiran, and Andreas Schreiber. Freezing and melting of water confined in silica nanopores. *ChemPhysChem*, 9(18):2651–2659, 2008.

[2] Hugo K Christenson. Confinement effects on freezing and melting. *Journal of Physics: Condensed Matter*, 13(11):R95–R133, 2001.

[3] J G Dash, Haiying Fu, and J S Wettlaufer. The premelting of ice and its environmental consequences. *Reports on Progress in Physics*, 58(1):115–167, 1995.

[4] Maxim Erko, Dirk Wallacher, and Oskar Paris. Deformation mechanism of nanoporous materials upon water freezing and melting. *Applied Physics Letters*, 101(18), 2012.

[5] Zhihong Liu, Ken Muldrew, Richard G. Wan, and Janet A. W. Elliott. Measurement of freezing point depression of water in glass capillaries and the associated ice front shape. *Physical Review E*, 67(6):061602, 2003.

[6] D. H. Everett. The thermodynamics of frost damage to porous solids. *Transactions of the Faraday Society*, 57:1541, 1961.

[7] Robert W. Style and Stephen S. L. Peppin. The kinetics of ice-lens growth in porous media. *Journal of Fluid Mechanics*, 692:482–498, 2012.

[8] MA Kessler and BT Werner. Self-organization of sorted patterned ground. *Science*, 299(5605):380–383, 2003.

[9] Albert F DiMillio. A quarter century of geotechnical research. Technical report, 1999.

[10] Hisashi Ozawa and Seiiti Kinosita. Segregated ice growth on a microporous filter. *Journal of Colloid And Interface Science*, 132(1):113–124, 1989.

[11] M. Vignes and K. M. Dijkema. A model for the freezing of water in a dispersed medium. *Journal of Colloid And Interface Science*, 49(2):165–172, 1974.

[12] Milon F George and Michael J Burke. Cold Hardiness and Deep Supercooling in Xylem of Shagbark Hickory 1. *Plant Physiology*, 59(2):319–325, 1977.

[13] Thomas J. Zabadal, Imed E. Dami, Martin C. Goffinet, Timothy E. Martinson, and Mark L. Chien. Winter Injury to Grapevines and Methods of Protection. *Michigan State University Extension*, E2930:1–44, 2007.

[14] Michael Wisniewski. An overview of cold hardiness in woody plants: seeing the forest through the trees. HortScience. *HortScience August 2003 vol. 38 no. 5*, 38(5):952–959, 2003.

[15] Soichi Arai and Agricultural Chemistry. *Biological ice nucleation and its applications*.

[16] Zoran Ristic and Edward N. Ashworth. Response of xylem ray parenchyma cells of red osier dogwood (Cornus sericea L.) to field feezing sress, and to feeze-thaw cycle. *Journal of Plant Physiology*, 149(6):735–745, 1996.

[17] Olivier Coussy. *Mechanics and Physics of Porous Solids*. 2010.

[18] George W. Scherer. Freezing gels. *Journal of Non-Crystalline Solids*, 155(1):1–25, 1993.

[19] Vinay Pagay, Michael Santiago, David A. Sessoms, Erik J. Huber, Olivier Vincent, Amit Pharkya, Thomas N. Corso, Alan N. Lakso, and Abraham D. Stroock. A microtensiometer capable of measuring water potentials below -10 MPa. *Lab on a Chip*, 14(15):2806, 2014.

[20] Kunio Watanabe. Relationship between growth rate and supercooling in the formation of ice lenses in a glass powder. *Journal of Crystal Growth*, 237-239(1-4 III):2194–2198, 2002.

[21] Olivier Vincent, Alexandre Szenicer, and Abraham D. Stroock. Capillarity-driven flows at the continuum limit. *Soft Matter*, 12(31):6656–6661, 2016.

[22] Frédéric Caupin. Escaping the no man's land: Recent experiments on metastable liquid water. *Journal of Non-Crystalline Solids*, 407:441–448, 2015.

[23] Matthew S Barrow, P Rhodri Williams, Hoi-Houng Chan, John C Dore, and Marie-Claire Bellissent-Funel. Studies of cavitation and ice nucleation in 'doubly-metastable' water: time-lapse photography and neutron diffraction. *Physical chemistry chemical physics : PCCP*, 14(38):13255–61, 2012.

[24] Stanley L Hem. The effect of ultrasonic vibrations crystallization processes.